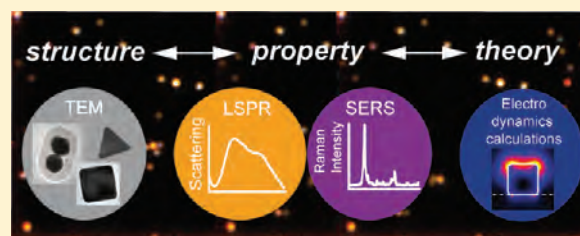


Correlated Structure and Optical Property Studies of Plasmonic Nanoparticles

Anne-Isabelle Henry,[†] Julia M. Bingham,[†] Emilie Ringe,[†] Laurence D. Marks,[‡] George C. Schatz,[†] and Richard P. Van Duyne^{*,†}

[†]Department of Chemistry and [‡]Department of Materials Science and Engineering, Northwestern University, Evanston, Illinois 60208-3108, United States

ABSTRACT: This article provides a review of our recent studies of single metal nanoparticles and single nanoparticle clusters aimed at correlating the structural and plasmonic properties of the *same* entity. The correlation between the structure and the optical properties arising from the localized surface plasmon resonance (LSPR) on single nanoparticles from various samples is described. Nanoparticles of different materials (Ag and Au) and shapes (spheres, cubes, triangles) are considered. Experiments were carried out using transmission electron microscopy (TEM), dark-field spectroscopy, and surface-enhanced Raman spectroscopy (SERS). Results of those measurements were compared with electrodynamic calculations to provide insight into the interpretation and physical meaning of the experimental results. We examine correlated studies of triangular nanoparticle arrays to highlight the significance of *single* entity measurements over ensemble-averaged measurements. Furthermore, we show how an examination of statistics on large data sets helps draw quantitative structure–LSPR relationships. We also show that implementing SERS in correlated measurements improves the understanding of factors important in determining SERS enhancements. Finally, we extend the scope of correlated measurements to the tracking and controlled manipulation of single nanoparticles, thus paving the way for *in vivo* diagnostics using nanomaterials.



I. INTRODUCTION

Nanoparticles have been the subject of intense research over the last two decades. A large variety of shapes (from “spheres” to complex anisotropic particles), sizes (from a few to > 100 nm), and materials (metals, semiconductors) can now be synthesized, thus broadening the range of the physical properties accessible, which can significantly differ from their bulk counterparts.^{1–3} In particular, metal nanoparticles have attracted special attention from synthetic and physical chemists. Numerous chemical and physical methods for the synthesis and fabrication of nanoparticles of controlled shape and size have been reported.^{4–13} At the same time, experimental and theoretical investigations of the physical (such as optical and magnetic) properties of nanoparticles have highlighted how they relate to the structure.^{1,14–17}

Materials such as Ag, Cu, Au, and Al with a negative real and small positive imaginary dielectric constant over a range of wavelengths are capable of supporting a surface plasmon resonance (SPR) when driven with UV–visible–NIR electromagnetic radiation. The SPR can be propagating or localized. Propagating surface plasmons are observed on thin metallic films, whereas localized surface plasmons are observed on nanoscale structures. Such materials are designated as plasmonic. In the case of metal nanoparticles smaller than the wavelength of visible light, the surface plasmon resonance is localized. The physical origin of this lies in the conduction electrons that oscillate coherently with the frequency of the applied radiation field. A theoretical description of linear optical properties like

extinction and scattering of a small spherical particle was proposed by Mie¹⁸ in 1908 for spherical particles. The extinction (absorption plus scattering) of a sphere of radius a with dimensions smaller than the wavelength of light can be expressed as

$$E(\lambda) = \frac{(1 + \chi)^2 8\pi^2 N a^3 \epsilon_{\text{out}}^{3/2}}{3\lambda \ln 10} \left[\frac{\epsilon_i(\lambda)}{(\epsilon_r(\lambda) + \chi\epsilon_{\text{out}})^2 + \epsilon_i(\lambda)^2} \right]$$

with ϵ_r and ϵ_i being the real and imaginary parts of the metal dielectric function, respectively, and χ a shape factor whose value is 2. Gans extended this work to Au¹⁹ and Ag²⁰ spheroidal particles; in this case, $\chi > 2$ and a is the equatorial radius.²¹ It is important to note that an analytical expression for the extinction is only known for spherical and spheroidal particles, so extinction must be determined numerically for other nanoparticle shapes. Note also that the localized surface plasmon resonance (LSPR) is sensitive to the surrounding medium through the external dielectric constant ϵ_{out} (and thus the refractive index, n_{out} as $\epsilon_{\text{out}} = n_{\text{out}}^2$). As a consequence, the LSPR can be used to probe changes in the refractive index (RI) and thus monitor the external environment, e.g., adsorbates, of the plasmonic particle. Measurements of RI changes have been successfully implemented in high-resolution biosensors^{22,23} and gas sensors.^{24,25}

Received: January 31, 2011

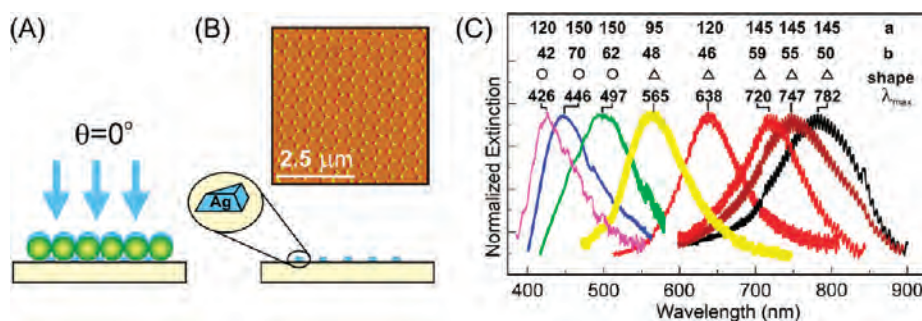


Figure 1. Nanoparticle array fabrication by NSL. (A) Metal is deposited at a specific angle, 0° here, onto drop-cast nanospheres. (B) Spheres are removed to yield a PPA (AFM image shown). (C) By changing sphere diameter, a , deposited metal thickness, b , or nanoparticle shape, the LSPR λ_{\max} can be tuned throughout the visible spectrum. (Adapted and reproduced from ref 7).

Another important feature of the LSPR is the intense electromagnetic field arising at the surface which assists surface-enhanced spectroscopies.^{26–29} The intensity of the Raman scattering of molecules lying at a particle surface is dramatically increased compared to the one usually observed in solution by Raman spectroscopy. The ratio of the surface-enhanced Raman scattering (SERS) intensity per adsorbed molecule to the normal Raman scattering intensity per bulk molecule is defined as the enhancement factor (EF) and quantifies the enhancing capability of a SERS-active structure.³⁰

Correlating structure and function is a powerful method for understanding the chemical and physical properties of an entity. While measuring the function—or property—of identical molecules in solution is representative of the sample, ensemble measurements may not reflect the properties of individual components when the individual components show significant dispersion. This is especially true of metal nanoparticle samples where the structure affects the optical properties and small structural inhomogeneities in the synthesized nanoparticle population have significant consequences. Indeed, we can expect that an ensemble measurement of nanoparticle optical properties does not reflect the spectrum of an individual entity, so structurally correlated single nanoparticle spectroscopy is an essential tool to understand the plasmonic properties of nanoparticles. To get single particle (or cluster) data one needs both single particle optical detection and single particle structural information.

Optical dark-field microscopy was developed at the beginning of the 20th century for the observation (count and size estimation) of metal colloids by Zsigmondy,³¹ who received the 1925 Nobel Prize in Chemistry for the development of the ultramicroscope and his studies of metal and other colloids. About ten years ago, the groups of Feldmann^{32,33} and Schultz^{34,35} independently performed the first spectroscopic studies of single metal nanoparticles. Mock et al. reported the correlation of structure to the LSPR spectrum of single nanoparticles when they performed dark-field spectroscopy and transmission electron microscopy (TEM) on Ag particles with various shapes.³⁵ This method has been demonstrated to be extremely powerful in probing the distribution of optical properties within a nanoparticle sample, and correlating structure and SERS activity of the same nanoparticle cluster has been crucial to modeling SERS, especially for understanding single molecule SERS (SMSERS).³⁶

In the present Feature Article, we describe correlated structural–optical–spectroscopic property studies performed on various plasmonic nanoparticle samples utilizing TEM, LSPR,

and SERS. This review is organized as follows: First, we describe in Section II macroscopic spatially correlated measurements of structure and LSPR on 2D periodic arrays of triangular particles. In Section III, we specifically address the correlation of structure and LSPR for single metal nanoparticles. Section IV is a discussion of the information that can be obtained from a statistical analysis of a large sample size. In Section V we present recent results from correlated TEM/LSPR/SERS studies on single SERS-active nanoparticle clusters. Finally, we define the limitations and discuss some applications offered by correlated studies of single metal nanoparticles.

II. BULK/ENSEMBLE CORRELATION METHODS

Getting accurate structural–optical property relationships from bulk measurements requires exquisite reproducibility of the individual plasmonic nanoparticles across a sample and from one sample to another. In the following section, we describe the fabrication of nearly identical structures over large areas and discuss the variations in LSPR spectra across these samples. Additionally, we review experiments on nanoparticle arrays to indirectly correlate structure and extinction measurements as well as to directly correlate extinction and SERS measurements.

a. Periodic Particle Arrays Fabrication by Nanosphere Lithography. Nanosphere lithography (NSL) is a proven lithographic method for fabricating nanoparticle arrays in an inexpensive and massively parallel way. The principle of the method is simple: first, spheres are self-assembled on a surface to serve as a mask; material is deposited through the sphere mask; finally, after removing the sphere mask (by sonication in solution), only a periodic particle array (PPA) remains on the substrate. The four experimental variables in NSL are: (i) the mask (i.e., sphere size and number of sphere layers),^{37,38} (ii) the deposition conditions⁷ (deposition time and rate to control the thickness, angle of deposition with respect to the surface, number of deposition steps), (iii) the substrate properties, and (iv) the deposited material (Figure 1A). While the first two parameters control the structure of the fabricated particles through the shape (triangular prisms, elongated particles, dots, and others⁷) (Figure 1B), lateral dimension, interparticle spacing, and thickness, the last two parameters allow the dielectric constant of the support (glass, mica, indium tin oxide, SF-10)^{7,39,40} and the materials (Ag, Au, Cu, and Al)^{37,41–43} to be tuned. Ultimately, the combination of tunable parameters considerably expands the structural variety and LSPR tunability of the structures fabricated by NSL (Figure 1C), and the LSPR λ_{\max} position can be tuned over the visible spectrum to the mid-IR.

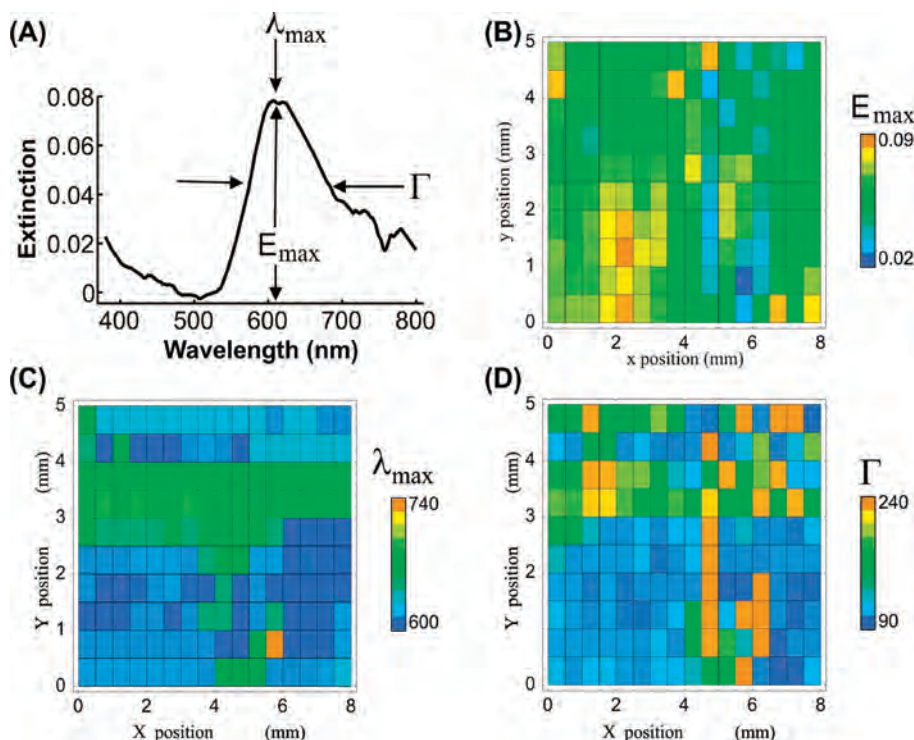


Figure 2. (A) Representative UV–vis extinction spectrum of a Ag nanoparticle array fabricated by NSL. Image maps are shown depicting the spectral variation across a 5×5 mm NSL area corresponding to the variation in E_{\max} (B), λ_{\max} (C), and Γ (D). (Reproduced from ref 50.)

The structural reproducibility within the array is limited by two factors: (i) the ability to organize the spheres homogeneously in a hexagonal close-packed array over the surface and (ii) the size dispersion of the spheres used for the mask. The use of nonfunctionalized silica or polystyrene nanospheres (~ 200 – 1000 nm in diameter) with a low dispersity in size (5–10%) ensures that areas as large as $500 \mu\text{m}^2$ are uniformly covered, permitting studies of plasmonic properties with microprobes. To get larger defect-free areas, i.e., to minimize the number of inherent defects such as dislocations and holes, deposition via convective self-assembly has been successfully demonstrated.⁴⁴ Stability issues such as a solvent-induced shape change from triangular to disk-like particles⁴⁵ can be tackled by using atomic layer deposition as a strategy to provide chemical⁴² and mechanical⁴⁶ protection of the metal nanoparticle arrays even at high temperatures (up to 300°C) with minimal effects on the optical and spectroscopic properties.

b. Correlated Structural–Optical Studies of NSL Fabricated Triangle Arrays. The LSPR properties of nanoparticle arrays made by NSL are routinely characterized by extinction spectroscopy. Fiber optic microprobes allow probing and collecting the extinction spectrum of areas as small as 2 mm in diameter. The small size of the interrogated areas compared to the substrate (~ 2 cm in diameter) allows the extinction to be probed over multiple areas and thus provides insight on the quality of the PPA over the substrate. In particular, extinction spectroscopy and atomic force microscopy (AFM) have been extensively used for indirect spatially correlated studies on NSL-fabricated structures.^{7,29,37,38,45,47,48}

An interesting illustration of the structure–LSPR correlation has been reported by Zhang et al.⁴⁹ who performed macroscale UV–visible extinction and AFM measurements. To modify the structure of Ag triangles made by NSL in a controllable manner

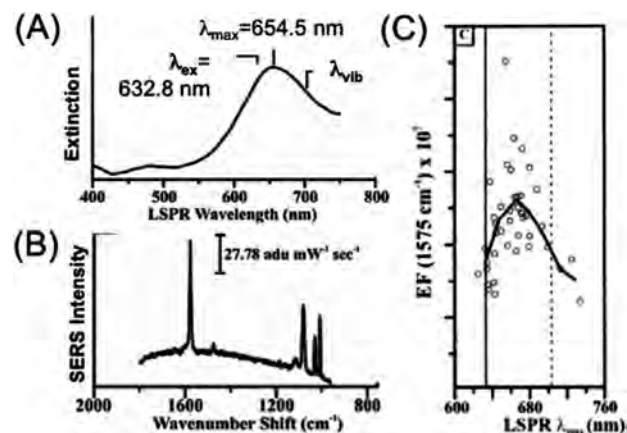


Figure 3. Spatially correlated study of NSL arrays. (A) Spatially correlated LSPR (extinction) and (B) SER spectra of the substrate dosed with benzenethiol. (C) Plasmon-sampled surface-enhanced Raman spectrum for the 1575 cm^{-1} band with a $\lambda_{\text{ex}} = 632.8$ nm excitation wavelength (solid line); the dashed line represents the Stokes frequency shift, λ_{vib} . (Adapted and reproduced from ref 40.)

and monitor the corresponding spectroscopic changes, the authors performed chronocoulometric experiments on Ag particles fabricated on a transparent and conductive substrate (indium tin oxide). They were able to monitor the shape evolution from triangular prisms to disks and identify the steps of the transformation mechanism. Under electrochemical oxidation, the extinction maximum exhibits a blue shift, as expected based on earlier measurements (Figure 1C).

To quantify the variations in the extinction spectrum of Ag particles over an entire substrate in a systematic way, Ormonde et al.⁵⁰

performed scanning UV–visible extinction spectroscopy on NSL fabricated triangle arrays. By scanning the substrate in two dimensions to measure the extinction on small areas (0.5×0.5 mm), the extinction maximum intensity (E_{\max}), position (λ_{\max}), and full-width at half-maximum (Γ_{\max}) of each area were measured. A typical spectrum for triangles using 400 nm diameter spheres and color maps for E_{\max} , λ_{\max} , and Γ_{\max} are presented in Figure 2. By defining a color scale for each parameter range of values (E_{\max} , λ_{\max} , and Γ_{\max}), every measured 0.5×0.5 mm area was attributed a color based on the deviation of the spectroscopic parameter from the expected spectrum for the fabricated triangles. Overall, scanning extinction UV–visible spectroscopy is a valuable tool to assess qualitatively the defects and quantitatively the LSPR properties of a metal nanoparticle array.

A further step in correlated studies of nanoparticle arrays has been achieved by Haynes and Van Duyne.⁴⁰ They carried out experiments to spatially correlate the optical (LSPR) and SERS properties on multiple Ag triangular particle arrays (Figure 3). The versatility of the experimental setup allowed the extinction (Figure 3A) and the SERS signal (Figure 3B) of the same region of the sample to be measured by interchanging the light and detection sources without moving the sample. Therefore this work investigated the fundamentals of the SERS electromagnetic effect by probing the SERS intensity, and thus the SERS EF, at different excitation wavelengths and tuning the LSPR of the substrate to the excitation wavelength (Figure 3C). The LSPR λ_{\max} distribution from domain to domain on the substrate was determined to vary with a Gaussian distribution having a standard deviation of ~ 10 nm. To identify the factor(s) accounting for this distribution, the structural variation of the triangular nanoparticles was carefully characterized by measuring their dimensions (lateral size and height) by AFM at different locations on the substrates. It was determined that the structures varied by $\sim 6\%$. Although this structural variation contributed to the LSPR λ_{\max} distribution as expected, it is clearly not the only factor to be considered. The comparison of two substrates differing in their hydrophilicity revealed that inhomogeneities in the local dielectric environment created by water adsorption were another factor accounting for the LSPR λ_{\max} variation. The optical and spectroscopic characterization through systematic measurement of the SERS EF, the LSPR λ_{\max} as a function of the excitation wavelength λ_{ex} and the molecular resonance wavelength λ_{vib} of the SERS target molecule permitted Haynes and Van Duyne (i) to show that NSL-fabricated substrates were SERS active and (ii) to establish some trends regarding the LSPR–SERS relationship. The plasmon-sampled SERS spectra clearly demonstrated that the maximum SERS EF occurs when the LSPR λ_{\max} lies between λ_{ex} and the Stokes frequency shift. These optimization conditions have been shown to be molecularly general by performing the same plasmon-sampled SERS experiments with different resonant molecules.

In summary, spatially correlated ensemble measurements of the extinction and the structure of nanoparticle arrays have demonstrated that not only the variations in structural parameters but also the presence of adsorbates in very small quantities have an effect on the LSPR spectrum. This correlation provides useful information for both synthesis and ensemble measurements. It should be noted that NSL-fabricated nanoparticles are identical on a relatively coarse scale, and the details of internal grain structure as well as corner rounding and other nanoscale structural elements vary across the sample. To further

elucidate the relationship between structure and LSPR spectrum features (λ_{\max} and line width), single nanoparticle measurements are necessary.

III. SINGLE NANOPARTICLE STUDIES

Single nanoparticle measurements have multiple advantages over ensemble-averaged measurements. First, single nanoparticles are easily implemented in multiplexed detection schemes since each unique nanoparticle possesses a distinguishable LSPR maximum. An additional advantage is that the absolute detection limit (number of analyte molecules per nanoparticle) is significantly reduced, leading us to the ultimate sensing limit: the single molecule.³⁶ A third advantage of single nanoparticle spectroscopy is the ability to measure the LSPR spectrum of individual particles with a high signal-to-noise ratio.⁵¹ Finally, single nanoparticle spectroscopy allows us to examine exactly which structure gives rise to which spectral properties. We can thus address some fundamental questions: Which structure is the most sensitive to local RI? How does the structure affect the plasmon frequency? Which structural parameters affect the plasmon width? By examining single nanoparticle spectra, these questions can begin to be addressed. Here, we describe the initial single nanoparticle spectroscopy experiments that provided the groundwork for single nanoparticle correlated studies.

A significant advantage of single nanoparticle spectroscopy is the ability to understand nanoparticle properties that are normally hidden in ensemble measurements. For example, the sensitivity of nanoparticles to the surrounding RI is essential for sensing experiments. Typically, this property had been exploited using nanoparticle arrays, and the RI sensitivity was averaged over hundreds of nanoparticles. Mock et al. were the first to investigate the sensitivity of the LSPR scattering spectrum of single nanoparticles by exposing them to different RI oils.⁵² However, the strength of LSPR sensing lies in the ability to detect *adsorbates* on nanoparticles. In 2003, Raschke et al.⁵³ and McFarland and Van Duyne⁵¹ independently reported the first single nanoparticle sensing experiments to examine the sensitivity to molecular adsorbates. Raschke et al. focused on single Au nanoparticles functionalized with biotin and the specific interaction with streptavidin,⁵³ whereas McFarland and Van Duyne examined the formation of self-assembled monolayers (SAMs) on single Ag nanoparticles as well as the bulk RI sensitivity of Ag nanoparticles.⁵¹

McFarland and Van Duyne utilized dark-field microscopy coupled with a spectrometer for optical analysis, a common technique for single nanoparticle spectroscopy, depicted in Figure 4A. Briefly, white light sent through a high numerical aperture (NA) dark-field condenser is used to illuminate the single nanoparticles. The NA is defined as $NA = n \sin \theta$, where n is the RI of the medium and θ is the half-angle of the maximum cone of light (Figure 4B). The dark-field condenser is equipped with a circular block at the lens such that a *hollow* cone of light is transmitted and focused at the sample to excite the nanoparticle plasmons. The nanoparticle scattered light is collected through a variable NA objective (set to a lower NA than the dark-field condenser) and sent to a CCD coupled to a spectrometer. The light illuminated through the condenser is at an angle higher than that prescribed by the NA of the objective. The illumination light is thus not collected by the low NA objective—only the light scattered by the nanoparticle; therefore, this is a “*dark-field*” configuration. To ensure single nanoparticle spectroscopy,

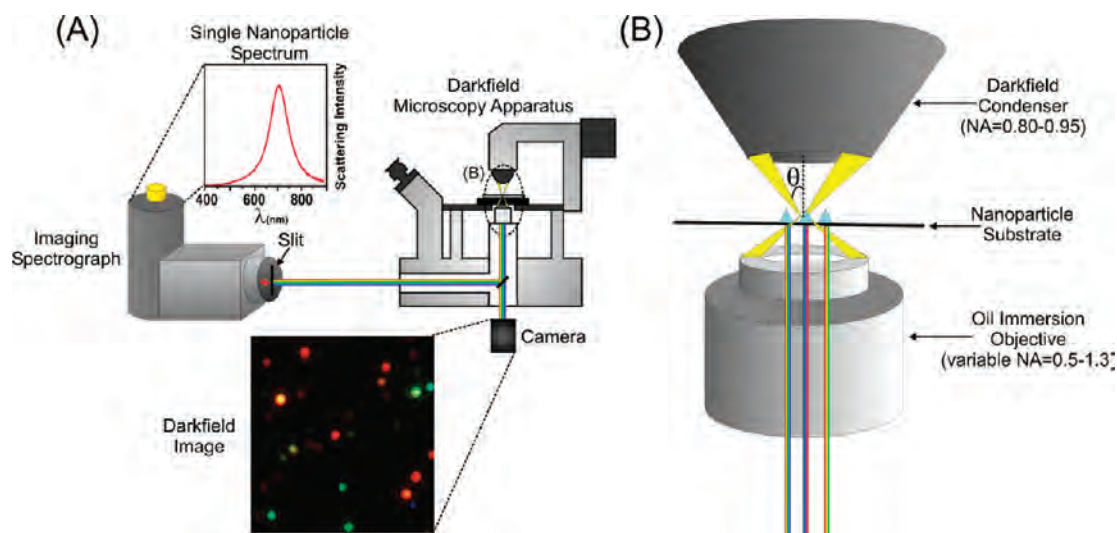


Figure 4. Single nanoparticle spectroscopy apparatus. (A) White light is brought in through a dark-field condenser to excite the LSPR of the single nanoparticles, and only the scattered light is collected by an oil immersion objective. The scattered light is sent either to a camera for imaging or through a slit to an imaging spectrograph. The slit ensures that light from only a single nanoparticle is sent through the spectrometer grating to yield a single nanoparticle scattering spectrum. The field of view of the dark-field image shown is $\sim 20 \mu\text{m} \times \sim 22 \mu\text{m}$. (B) Closeup of the dark-field condenser and objective.

a single nanoparticle is isolated in the center of the slit of the spectrometer such that no other nanoparticles are in the field of view. This process is repeated for each subsequent nanoparticle of interest.

Single Ag colloidal nanoparticles were used to determine the RI response to both solvent environment and adsorbates. For example, three different single Ag nanoparticles demonstrated RI sensitivities varying by a factor of ~ 1.5 when exposed to different solvents. On the basis of prior work examining single nanoparticle scattering spectra,³⁵ it was inferred that the particles exhibiting RI sensitivities of 161 nm/RIU, 197 nm/RIU, and 235 nm/RIU were spherical, triangular, and rodlike, respectively. That is, the particle with the highest aspect ratio exhibited the highest RI sensitivity, consistent with Mie Theory.¹⁸ In an ensemble measurement, such observations are not possible because only the average RI sensitivity is measured.

To investigate the sensitivity of single nanoparticles to adsorbate molecules, the formation of an octanethiol monolayer was observed in real-time by monitoring the shift in λ_{max} of the scattering spectrum. The λ_{max} response exhibited first-order kinetics with a rate constant of 0.0167 s^{-1} . When Ag nanoparticles were incubated in a hexadecanethiol solution, the λ_{max} redshifted by 40.7 nm, corresponding to $<60\,000$ adsorbate molecules on the surface, demonstrating zeptomole sensitivity.⁵¹ Finally, a linear relationship between the LSPR response and the SAM alkyl chain length was observed for multiple single Ag nanoparticles that had a similar plasmon frequency, and it was concluded that the RI sensitivity was consistent with that of platelets or disks. This work demonstrates that the same types of sensing experiments performed on plasmonic arrays can be performed on single plasmonic nanoparticles. Additionally, because the spectra are not part of ensemble measurements, structural information can be inferred from the single nanoparticle spectra. Sensing experiments like those by McFarland and Van Duyne helped clarify the relationship between structure and spectrum without correlated data. The size and shape variation in a citrate-reduced Ag colloid synthesis is beneficial to examine the wide range of structures available. However, by focusing on a

more monodisperse nanoparticle sample, a clearer picture of structural and spectral correlation can be drawn.

Work by Sherry et al. focused on the single nanoparticle spectroscopy of nanocubes⁵⁴ and triangular nanoprisms.⁵⁵ The authors demonstrated that although similar shapes were present in a single sample, as observed by TEM measurements, a variety of single nanoparticle LSPR scattering spectra were measured, further emphasizing the significance of single nanoparticle spectroscopy. The RI sensitivity was determined for multiple single nanoparticles, revealing additional structural details of the nanoparticles, like corner rounding.

While comparing the ensemble LSPR spectrum of Ag nanocubes (in water) to that of a single Ag nanocube on a glass substrate (submersed in water), a striking difference was observed: the single particle spectrum consisted of two discrete peaks, whereas the ensemble spectrum consisted of primarily a single peak (a small peak around 350 nm was attributed to residual particles in solution). To clearly understand the physical origin of those peaks, finite difference time domain (FDTD) calculations were performed for a cube in a variety of media. The FDTD results for cubes immersed in water or laying on a dielectric substrate both gave rise to a spectrum containing two peaks, indicating the multimodal resonance origin of the peaks. The high-energy peak is a quadrupolar resonance that becomes prominent when a Ag cube is in a relatively high RI medium, i.e., as low as 1.33 (water). Considering the fact that the configuration of a cube lying on a surface is a nonsymmetric environment, the resonance is not a true quadrupole, just as the dipole is not a true dipole. Figure 5 shows a simulated spectrum of a single nanocube on a dielectric substrate. The higher-energy peak (quadrupolar in origin), designated as peak A (distal) in Figure 5, has strong correlations with enhanced electric fields away from the surface, whereas the lower-energy peak (dipolar in origin), peak B (proximal) in Figure 5, correlates with fields toward the substrate. Clearly, single particle studies on metal nanoparticles (as Ag cubes,⁵⁴ Ag triangular particles,⁵⁵ Au rods,³³ and Au nanoshells⁵⁶) have considerably facilitated the discrimination of the factors affecting the LSPR spectrum, in particular effects

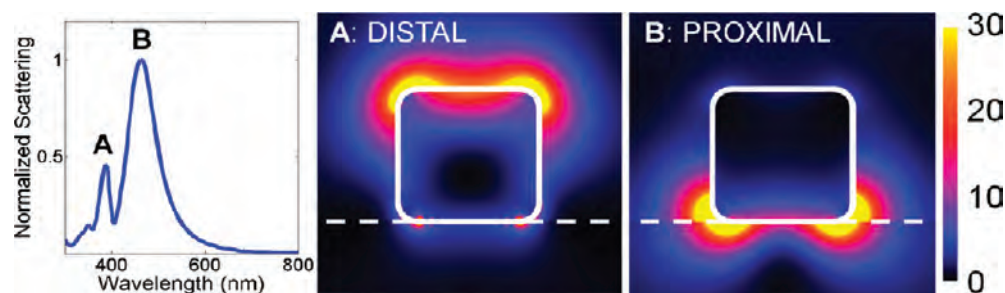


Figure 5. FDTD modeling showing the scattering spectrum of a single nanocube (face-to-face distance: 78 nm) on a $n = 1.5$ substrate. The field intensities for the distal (A) and the proximal (B) peak. (Reproduced from ref 72.)

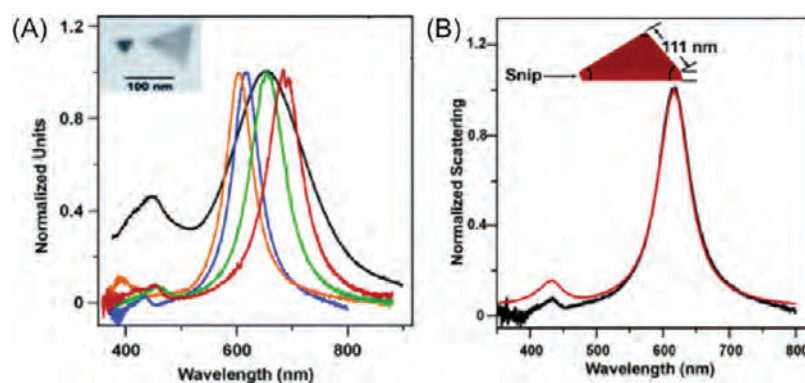


Figure 6. Triangular nanoprism LSPR spectra. (A) Ensemble (black) extinction spectrum of single triangular nanoprisms overlaying four single triangular nanoprism scattering spectra (color), both in an aqueous environment. The inset is a representative TEM image of the triangular nanoprisms. (B) Experimental (black) and DDA modeled (red) single nanoprism scattering spectra. The DDA modeled spectrum used a 111 nm edge length, 15 nm tip sharpness, and 10 nm height for calculations. (Reproduced from ref 55.)

related to high RI environments such as the presence of a substrate.

As mentioned previously, an additional measurable parameter characterizing nanoparticles is the RI sensitivity. The single Ag nanocubes on a substrate provide an interesting example due to the presence of two plasmon peaks. It is expected that the higher-energy peak (peak A in Figure 5) would have a higher RI sensitivity than the lower-energy peak (peak B in Figure 5) since peak A has most of its electric field probing the bulk material. This occurs even though this resonance has quadrupole character, which due to the shorter range of quadrupole fields has an intrinsically lower RI sensitivity. Although the results agreed qualitatively with what was expected, peak A shifted less than predicted by theory. It was hypothesized that the cube corners immersed in the bulk environment were “annealed” by the solvents utilized in the RI study more than the corners touching the substrate. This explanation is consistent with prior work^{51,57} that demonstrated particle corners with larger radii of curvature are less sensitive to changes in the RI. The unexpected observation of lessened RI sensitivity offered insight into the structural nuances of single nanoparticles, which would be otherwise obscured by ensemble measurements.

In the triangular nanoprism study by Sherry et al.,⁵⁵ Ag nanoprisms were synthesized using the procedure pioneered by the Mirkin group in which small spheroidal seed particles are converted into triangular nanoprisms through a photomediated mechanism.⁶ TEM measurements depicted largely triangularly shaped nanoprisms, albeit with varied sizes. Figure 6A illustrates single nanoparticle spectra of multiple nanoprisms in comparison

to the ensemble spectrum. It is observed that the single nanoprism spectra are narrower than the ensemble spectrum, as expected from inhomogeneous broadening, and that the single nanoprism spectra cover a range of wavelengths. The different spectra are presumably from triangle-like nanoparticles with different sizes. To further understand the effect of structure on the scattering spectrum, discrete dipole approximation (DDA) modeling was used. A triangular nanoprism which had a $\lambda_{\text{max}} \sim 620$ nm was matched to a modeled triangular nanoprism with an edge length = 111 nm, tip sharpness (corner truncation) = 15 nm, and height = 10 nm (Figure 6B). The combination of theory and experiment helped elucidate the structural–spectral relationship. Although the nanoprism shapes are largely triangular, there is significant variation in nanoparticle size and tip sharpness. It was concluded that these variations give rise to different scattering spectra. Although these studies were performed on single triangular nanoprisms in a known size range, the dimensions of each particle in these measurements were not known.

To fully elucidate the origin of fine spectral details such as the plasmon width and frequency, single particle correlated structural–optical characterization is necessary. In particular, there is a need to spatially correlate optical and structural measurements on single plasmonic nanoparticles in parallel and in real-time. A novel method utilizing through-the-objective white light total internal reflection (TIR) for LSPR and AFM measurements was achieved by Stiles and Willets et al.⁵⁸ This method is analogous to the TIR fluorescence (TIRF) microscopy technique using laser excitation.^{59,60} A schematic is depicted in Figure 7A. Briefly,

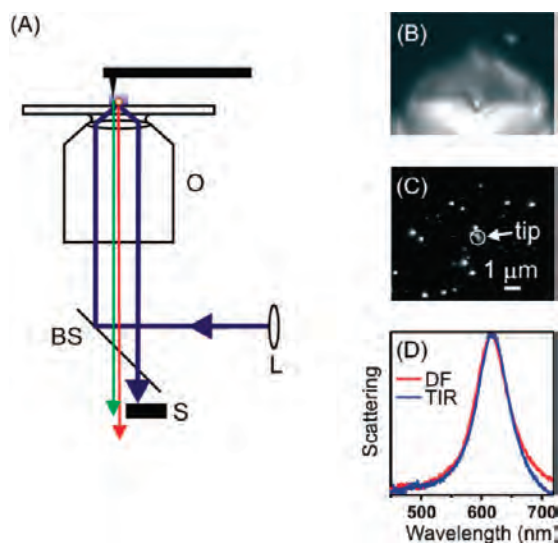


Figure 7. (A) Schematic of the through-the-objective white light TIR apparatus for single nanoparticle spectroscopy and AFM. White light from a tungsten-halogen lamp is directed through a lens (L) to a beam splitter (BS) and through a TIRF objective. A metal beam stop (S) is used to block the 50% of the TIR light that is transmitted through the beam splitter. Dark-field single nanoparticle scattering images when the AFM tip is in contact with the sample using (B) a traditional dark-field configuration (see Figure 4) and (C) the through-the-objective TIR approach. (D) Single nanoparticle scattering spectra comparing the traditional dark-field method (DF) in red and the TIR method in blue.

white light is sent through a high NA objective off-axis such that the light is bent at high enough angle to achieve TIR. The nanoparticle LSPR excitation occurs by an evanescent wave generated at the air–sample interface, and the scattered light is collected by the same objective. The through-the-objective approach is necessary for these spatially correlated measurements using AFM. When traditional dark-field geometries are utilized (dark-field condenser as described earlier in this section), the AFM tip scatters so intensely that the diffraction-limited spots from the nanoparticles are obscured (Figure 7B). However, using the through-the-objective white light TIR configuration, clear dark-field scattering images are obtained, even when the AFM tip is in contact with the sample (Figure 7C). This is the result of an evanescent wave that exponentially decays in intensity in the z -direction, allowing the AFM tip to be in contact with the sample and no background scattering from the cantilever. This through-the-objective white light TIR technique allows a single nanoparticle scattering spectrum to be measured, while the AFM tip is in contact with the nanoparticle (Figure 7D). This novel method using through-the-objective white light TIR not only correlated structural and optical measurements of single triangular nanoprisms but also elucidated the effect of certain tip–nanoparticle interactions on the optical properties. For example, it was determined that a water meniscus was forming between the AFM tip and the nanoparticle, mechanistic principle mechanism of dip-pen nanolithography (DPN).^{61,62} This work demonstrated a novel method to spatially correlate optical and structural measurements, offering insight into the structural–spectral relationship as well as tip–particle interactions.

In summary, dark-field spectroscopy offers the technical ability to measure scattering from a *single* nanoparticle. As a result, optical information that is otherwise being hindered by the

ensemble in extinction measurements is now measurable. Substrate and RI effects on metal nanoparticles can now be studied with unprecedented sensitivity. An alternative method, the through-the-objective white light TIR technique, enables the direct correlation of structure (measured by AFM) and LSPR.

IV. SINGLE NANOPARTICLE STUDIES: STATISTICS OVER LARGE POPULATIONS

Single particle correlated measurements are paramount to unraveling structure–function relationships, as described thus far. Electron microscopy techniques have been used to perform such experiments. While scanning electron microscopy (SEM) can be used as a structural characterization tool (e.g., for triangles⁶³ and decahedra^{35,63,64}) the resolution is generally no better than 1 nm, and TEM yields micrographs of much higher resolution. Experimental challenges related to this approach are surmounted by using TEM grids as substrates for the dark-field microscopy scattering measurements,^{65,66} allowing transfer of the sample into a transmission electron microscope, in which subnanometer resolution images can be routinely acquired. Additionally, the asymmetric center of the grid used provides an origin to establish a coordinate system for easy positioning. Using this technique, the scattering spectrum and structure of a single Ag nanocube were obtained,⁶⁶ confirming previous results⁵⁴ which indicated the presence of two plasmon modes. Precise measurements of the face-to-face distances and corner rounding from TEM images could be used in FDTD calculations, yielding an impressive theory–experiment match. Additional FDTD calculations predicted a redshift of the plasmon for increasing size and decreasing corner rounding.

a. Au and Ag Nanocubes. Quantification of structure–function relationships is critical to the advancement of plasmonics, as structure provides a powerful handle on optical properties. Predictive rules would allow quick, hassle-free decision on parameters required to get any specific plasmon resonance frequency, for applications in optics and sensing. A way to fully elucidate this relationship is to take a statistical approach to correlated spectral and structural measurements. Previous experimental results concentrated on one up to tens of particles^{35,63,66} and heavily relied on calculations to give clues on factors contributing to the plasmonic properties of nanoparticles, such as size, shape, and dielectric environment. With sufficient data, it is possible to experimentally assess such factors and get results at a level unachievable by calculations. In addition, new trends or insight can be serendipitously discovered. Sets of correlated single particle data have recently emerged for Au decahedra,⁶⁷ Au spheroids,⁶⁸ Ag triangular plates,^{69,70} and Ag–Au cages.⁷¹ The high throughput achievable with the correlated LSPR/TEM technique described earlier allows acquisition of large data sets with exceptional spectral and structural precision: margins of errors on both the plasmon peak and nanoparticle size are of the order of 0.5 nm.

Using correlated LSPR/TEM, the effect of size, corner rounding, composition, and substrate dielectric medium on the plasmon resonance of nanocubes was experimentally addressed.⁷² Figure 8A presents LSPR frequency as a function of side length for Ag and Au nanocubes with aspect ratio 0.9–1.11 on either a polymer (polyvinyl formal, RI $n = 1.5$) or a semiconductor (Si_3N_4 , $n \sim 2$) substrate. For the nanocubes, the sharp, quadrupole-like high-energy peak is labeled distal, whereas the broader, dipole-like peak is referred to as proximal because of the

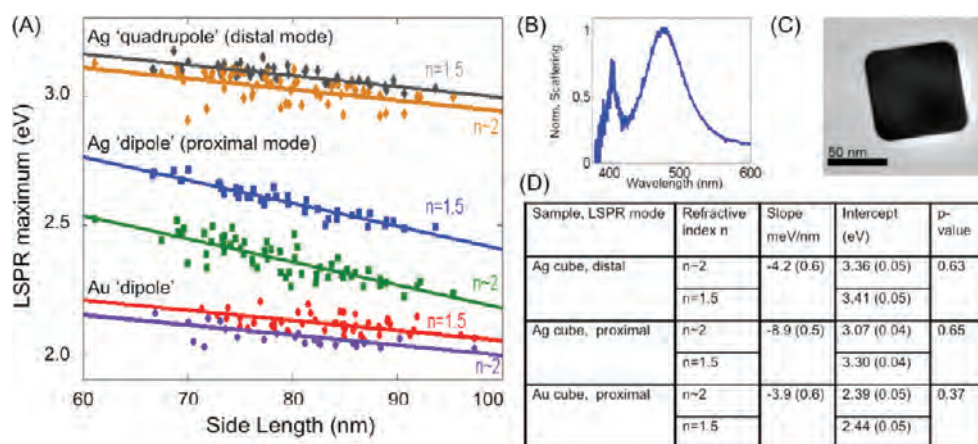


Figure 8. Statistical approach to correlated LSPR/TEM measurements on Ag and Au nanocubes on polyvinyl formal ($n = 1.5$) and Si_3N_4 ($n \sim 2$). (A) LSPR energy for the single proximal mode of Au and the proximal and distal modes of Ag. (B), (C) Examples of single particle spectral and structural data, respectively, for a Ag cube. (D) Results from analysis of covariance (ANOCOVA). The standard deviations are shown in parentheses.

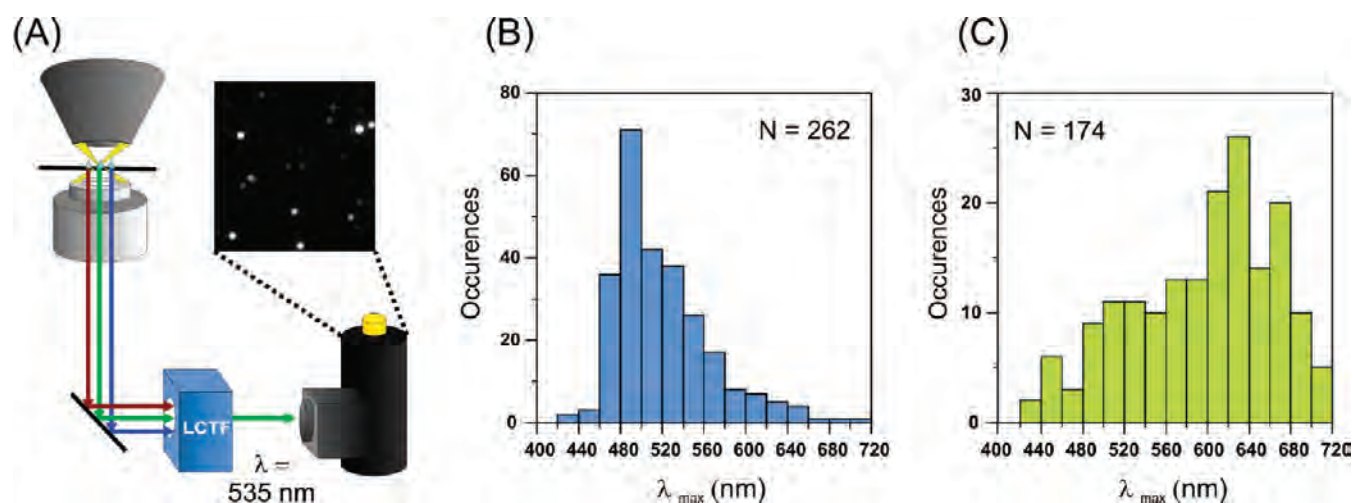


Figure 9. (A) Wide-field LSPR imaging experimental apparatus. Scattered light from the nanoparticles is sent through an LCTF, where only the specified wavelength of light is transmitted (535 nm shown here) to the CCD. (B), (C) Plasmon peak energy (λ_{max}) distribution for Ag colloids and Ag nanoprisms, respectively. (Reproduced from ref 76.)

symmetry of the field profiles, as illustrated in Figure 5 for a Ag cube. The first trend obvious in Figure 8A is the redshift of the plasmon with increasing size, which can be explained by retardation effects. Simply put, the plasmon resonance frequency changes with dimension because the electron oscillation has to accommodate the difference in electromagnetic phase between one end of the particle and the other (i.e., radiative depolarization effects).⁷³

Out of the 175 nanocubes analyzed, several statistically significant trends emerged. First, the composition (Ag or Au) not only influences the position of the plasmon for a given particle dimension but also dictates the LSPR frequency dependence on size and dielectric environment. This is due to the difference between various aspects of the dielectric functions of Ag and Au. Indeed, the shift for a given size is due to the magnitude of ϵ_r according to Mie theory;¹⁸ the composition-specific dependence on size is due to the electric scattering coefficient (a function of both the real and imaginary parts of the dielectric function);⁷³ and the different dependence on environment is due to the real part of the dielectric function and its derivative.⁷⁴ It is interesting to note that in this study the

substrate has no statistically significant effect on the size dependence of the LSPR energy for the three LSPR modes studied (Ag distal, Ag proximal, and Au proximal; vide supra). An effect, although small, is predicted from the explicit dependence of the electric scattering coefficient on the dielectric constant of the surrounding medium.⁷³ Another trend observed is the different size dependence of the energy of the proximal and distal modes for Ag nanocubes. The slope of the proximal resonance is approximately twice that of the distal one, as expected for dipolar and quadrupolar resonances. The Ag plasmonic modes also have disparate sensitivities to the RI of the substrate. Quadrupole modes tend to be less affected by the medium around them, and more importantly, the fields for the high-energy modes sample much less of the substrate than the fields for the lower-energy mode (Figure 5).

Not only can these trends be observed but also with the statistical approach to correlated LSPR (Figure 8B)/TEM (Figure 8C) they can be quantified at a level never achieved before and tested for statistical significance. Results of analysis of covariance (ANOCOVA) are presented in Figure 8D. Note that

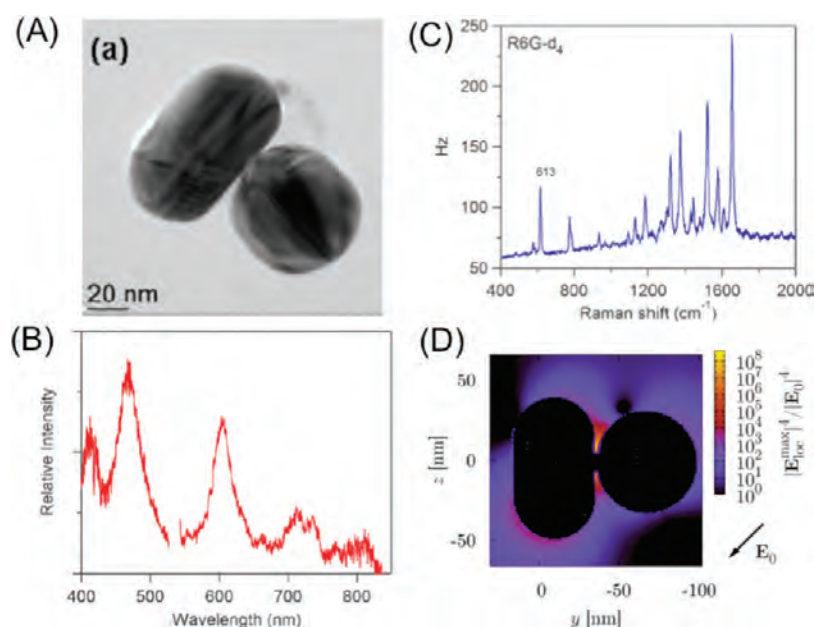


Figure 10. (A) Correlated TEM image, (B) LSPR scattering spectrum, (C) SER spectrum of rhodamine 6G on a sphere–rod dimer presented in panel (A), and (D) electric field contour map of a sphere–rod dimer modeled using DDA. (Reproduced from ref 79.)

the p -value is related to the probability that the difference between two groups is the result of chance, which goes from zero (not likely or, in other words, a real effect) to one (extremely likely). The size dependence of the LSPR energy was thus found to not be statistically different for a given peak on either substrate, despite previously discussed predictions. The small standard deviations on these results suggest that they are at a level where they can challenge and help improve theory. It can be seen that the dependence of the LSPR position on nanocube size is greatest for the Ag proximal LSPR, followed by Ag distal, and then by Au proximal. Perhaps the most novel result to come out of this statistical approach to LSPR/TEM measurements is that the quantitative nature of it can be used to predict LSPR positions of nanocubes over a large range of sizes and of different compositions (Au or Ag), as well as on different substrates (polyvinyl formal or Si_3N_4).

b. Plasmon Distribution. All experimental results presented thus far have been obtained by collecting the scattering spectrum of one particle at a time, centering the individual particle on the detector slit, a method arguably time-consuming and of limited applicability. Recently, Louit et al.⁷⁵ acquired spectra of metal nanoparticles diffusing in live cells by using a translation stage to compensate for the motion of the nanoparticles, paving the way for a new approach to dark-field microscopy. We have adapted a similar method to our needs by coupling an inverted microscope, equipped with a dark-field condenser (NA = 0.80–0.95) and a variable NA objective (NA = 0.5–1.3, set at NA = 0.5), with a liquid crystal tunable filter (LCTF) and a LN_2 -cooled CCD detector^{76,77} (Figure 9A). In this configuration, the scattered light from all the particles in a $\sim 20 \mu\text{m} \times \sim 50 \mu\text{m}$ area can be collected one wavelength at a time by scanning the LCTF. The scattering intensity of each diffraction-limited spot can then be integrated as a function of wavelength to construct single nanoparticle spectra.

The inherently high throughput of this wide-field LSPR imaging instrument allows unbiased sampling of nanoparticle scattering spectra. We have used this capability to study the plasmon peak distribution of two different reaction products, Ag

colloids and Ag nanoprisms, which were synthesized according to the procedure developed by Lee and Meisel⁷⁸ and Jin et al.,⁶ respectively. From TEM observations, we know that there is a variation in size and shape in the Ag colloids, and their plasmon peak distribution (Figure 9B) indeed reflects this inhomogeneity. Although TEM has shown the triangular nanoprisms to be relatively monodisperse, significant variation is observed in the scattering spectra, seen in the corresponding plasmon distribution (Figure 9C). Such histograms were the first demonstration of the high throughput capabilities of the new wide-field LSPR imaging setup, which is a promising new experimental approach.

V. CORRELATED SINGLE NANOPARTICLE SPECTROSCOPY FOR SERS

The LSPR excitation of metallic nanostructures produces an electromagnetic field at the surface of the particle, capable of enhancing ($>10^6$) the Raman scattering of molecules located in the vicinity of the surface, i.e., at an electromagnetic hotspot.^{21,79} SERS, which relies on this phenomenon discovered more than 30 years ago,⁸⁰ combines the selectivity of Raman spectroscopy (based on unique vibrational features of the molecule) with high sensitivity. Indeed, signals from single molecules have been detected.^{36,81} Although the fundamentals of the electromagnetic mechanisms are relatively well-known,^{27,82,83} some uncertainty has remained on the exact structure of the electromagnetic “hotspot” giving rise to the very high enhancements exploited in SMSERS. Not surprisingly, correlating structure and SERS activity has been of great interest in the SERS community.

Brus and co-workers have shed some light on this subject by performing correlated AFM and dark-field spectroscopy studies to measure LSPR and SERS on the same nanostructures, namely, Ag nanoparticles aggregated on a surface.^{84,85} They made several key observations. First, SERS signal is only measured from aggregates, (i.e., at least two particles), thus likely arising from the junction of nanoparticles. The resolution achieved by AFM images, though, was not sufficient to provide insights into the

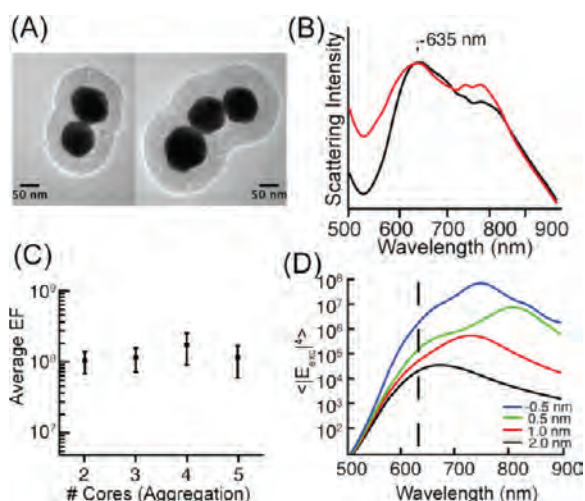


Figure 11. Correlated structural and optical characterization of individual SERS nanoparticle clusters (“nanoantennas”). (A) TEM images of a Au–SiO₂ core–shell dimer and trimer nanoantennas functionalized with Raman-active target molecules. (B) LSPR scattering spectrum of the dimer (black line) and the trimer (red line) in panel (A). (C) Average EF as a function of the aggregation state in nanoantennas. (D) Average electromagnetic enhancement from FEM calculations for different gap distances of the cores in a trimer, as a function of the wavelength. (Adapted and reproduced from ref 87.)

structure of the junctions. Second, they observed no correlation between the LSPR maximum position, λ_{max} and the SERS EF. In the following, we describe our recent results from the correlation of (SM)SERS, LSPR, and TEM at the single particle level.

a. SMSERS–LSPR–TEM Correlation. To identify with precision the structure of the hotspots capable of enhancing SERS-active single molecules, Camden et al.⁷⁹ performed correlated high-resolution TEM/LSPR/SMSERS experiments on aggregated Ag colloids. By starting with the experimental setup used for single particle correlated experiments (Figure 4), they incorporated instrumentation (laser, optics, spectrometer)⁸¹ to perform SERS on single nanoparticles and thus to perform TEM (Figure 10A), LSPR spectroscopy (Figure 10B), and SERS (Figure 10C) on the same Ag colloid aggregates incubated with rhodamine 6G. Also, by using the experimental dimensions as input for electrostatics calculations (DDA), they were able to get the contour plot of the electric field map, which clearly indicated that the hotspot was located on each side of the junction when the two particles were touching (Figure 10D). Note that the scattering spectrum that is presented in Figure 10B probably has some contributions from nanoparticle aggregates located in the diffraction-limited spot centered on the dimer of interest. From this correlated TEM/LSPR/SERS study and DDA calculations, it appears that the wavelength of the LSPR maximum is not correlated to the SMSERS excitation wavelength and that multiple aggregate structures are suitable to observe SMSERS. Very recent results from Kleinman et al.⁸⁶ using similar correlated measurements with another Raman chromophore (Crystal Violet) confirmed those conclusions while expanding the generality of SMSERS.

b. Single Particle SERS–LSPR–TEM Correlation. Reproducible and rational structures that can be studied by LSPR spectroscopy and SERS at the single nanoparticle/nanoaggregate level provide insight into the structure–plasmon–SERS intensity relationships. By using the same experimental method as Camden et al.,⁷⁹ Wustholz et al.⁸⁷ have performed correlated TEM–LSPR–SERS studies on

controlled SERS-active nanoparticle clusters. This study utilized aggregated spherical Au cores (~100 nm in diameter) on which Raman active target molecules were adsorbed (submonolayer coverage) (Figure 11A). The whole structure was then encapsulated in a SiO₂ shell (~50 nm thick) that provided (i) chemical and structural stability and (ii) the possibility to functionalize the surface with molecules for biologically related applications.⁸⁸ The diversity in nanoparticle clusters (number of cores per cluster and relative geometry of the cores)⁸⁹ allowed the exploration of fundamental questions such as: How does the number of cores affect LSPR maximum position and SERS activity? What is the most enhancing structure? How do LSPR maximum and SERS EF activity relate? What is the fine structure of the hotspot? The Wustholz et al. studies demonstrated experimentally that no specific type of nanoparticle cluster (dimers, trimers...) exhibited unique features in this particular population of clusters. In other words, two dimers can have very different spectra, whereas one dimer and a trimer can have very similar spectra (Figure 11B). Finite element method (FEM) calculations have greatly helped in addressing the dramatic effect of very small (–0.5 to 2 nm) intercore distances on the LSPR spectrum and the EF (Figure 11D). As for how LSPR and SERS EFs relate, this work confirmed that the LSPR maximum wavelength and the EF are not correlated, as earlier reported by Brus and co-workers.⁸⁴ The average SERS EF (averaged over the entire nanoparticle cluster aggregate, not only the supposed hotspots) was remarkably constant relative to the number of cores within the cluster (Figure 11C). Also, the range of experimentally measured maximum EFs was relatively low (factor of 70 from maximum to minimum) and is in very good agreement with the range predicted by FEM calculations at this excitation wavelength. The theoretical results identified the regions of high electromagnetic field in dimers and trimers.^{87,90} In the case of a trimer, the two hotspots were the regions located around each intercore junction.⁸⁷ To gain insight into the structure of the hotspot, diverse nanoparticle clusters were observed using HRTEM within the same sample. Two types of structures were identified, depending on whether the cores were isolated (i.e., separated by 0.4–1 nm) or slightly fused. In both cases, the dimensions measured are in the range predicted by theory to still provide enhancements in the 10⁸ range. Such correlated measurements of SERS, LSPR, and structure have allowed us to understand the detailed structure–activity relationship in hotspot containing nanoparticle clusters. The structure of the intercore region was shown experimentally and theoretically to have dramatic effects on the LSPR but only very moderate effects on the EF, for which the highest value measured was 4×10^8 .

By incorporating SERS measurements to spatially correlated structural–optical measurements at the single particle (here, single nanoparticle aggregate) level, new insights into fundamental questions relating LSPR and SERS as well as the structure of the hotspot have been obtained.

VI. CORRELATED STUDIES: APPLICATIONS AND LIMITATIONS

a. Single Particle Tracking. With emerging techniques and abilities to optically and structurally correlate hundreds of single nanoparticles, questions regarding utility and practicality arise. It is important to know exactly how minute structural parameters affect spectral properties, like plasmon frequency and width. With thorough characterization, these relationships can begin to be uncovered. This is extremely important on a fundamental level, but also for sensing applications. Continuing single

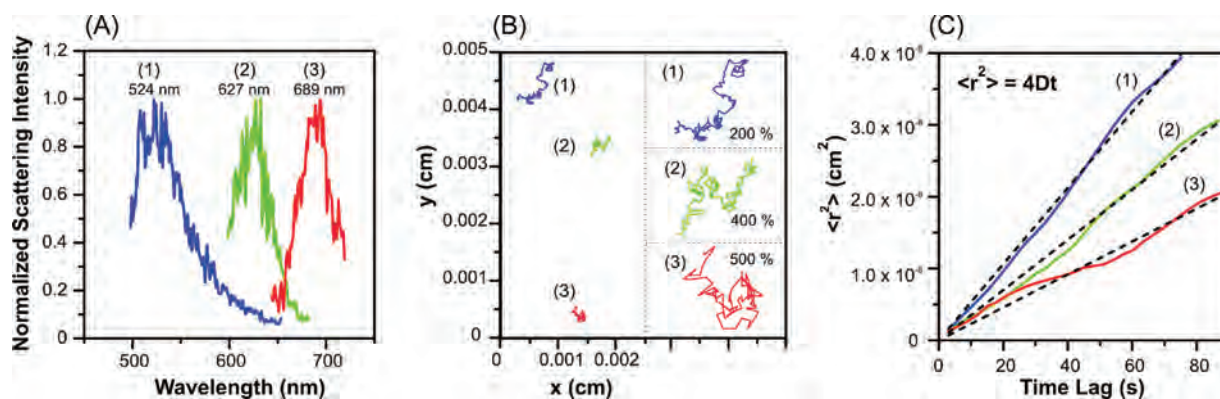


Figure 12. Characterization of three moving single nanoparticles. (A) Normalized scattering spectra of particles 1, 2, and 3 which have λ_{\max} of 524, 627, and 689 nm, respectively. The spectra were obtained, while the nanoparticles were moving according to the trajectories in panel B. (B) Single particle trajectories of particles 1, 2, and 3. (C) Plots of the mean square displacement $\langle r^2 \rangle$, which were calculated from the single particle trajectories in panel B, as a function of time lag, t . (Reproduced from ref 76.)

nanoparticle studies will further elucidate the relationship between structure and sensing capability.

A particular advantage of single nanoparticle studies is that they are not restricted to surface-bound geometries; that is, single nanoparticles can be investigated while they *move*. This is particularly significant for the biological community because single particle tracking provides new information on cell membrane organization, biomolecule movement on the cell surface, and the effects of the external cell environment.^{91–97} Single particle tracking is used to determine the diffusion coefficients of individual particles, allowing for modes of motion inside cells to be characterized. This technique has been utilized for single fluorophores, quantum dots, and plasmonic particles; however, it has been a challenge to measure the optical properties of a single particle simultaneously with its movement. Recently, Bingham et al.⁷⁶ utilized the wide-field imaging method described in Section IV to address this challenge.

The wide-field imaging technique utilizes dark-field microscopy with an LCTF to measure the resonant Rayleigh scattered light from multiple nanoparticles (*vide supra*). The intensity is integrated over multiple frames to build the scattering spectrum of many single nanoparticles simultaneously. Not only does each intensity frame have wavelength information but also it has time information, since the LCTF was scanned with a specific time interval. This feature made it possible to measure moving particles because the location of each particle at a given time in the wide-field image was known, allowing diffusional dynamics of moving particles to be characterized (Figure 12). The LSPR scattering spectra and the single particle trajectories of three single nanoparticles are displayed in Figure 12A and 12B, respectively. The mean square displacement ($\langle r^2 \rangle$) was calculated from the nanoparticle trajectories and plotted as a function of time lag, t (Figure 12C), demonstrating a linear relationship (slope $4D$, where D is the diffusion coefficient), indicative of Brownian diffusion. From the linear fit in Figure 12C, particles 1, 2, and 3 were determined to have diffusion coefficients of 1.33×10^{-10} , 8.75×10^{-11} , and 5.73×10^{-11} cm^2/s , respectively. Using the Stokes–Einstein relationship, the nanoparticles were found to have sizes within a factor of ~ 2 – 3 of the actual nanoparticle size of 80–100 nm.⁶

Due to camera limitations, a viscous environment (supersaturated aqueous glucose solution) was necessary for these single particle tracking experiments.⁷⁶ However, with an electron-multiplying (EM) CCD, single particle tracking was possible in water due to the decrease in required acquisition time. This improved the

technique such that a larger range of biologically relevant time scales are accessible. Two single nanoparticles with $\lambda_{\max} \sim 570$ and 621 nm were tracked in water and were determined to have diffusion coefficients of 9.0×10^{-8} cm^2/s (corresponding to 24 nm radius) and 6.3×10^{-8} cm^2/s (corresponding to 34 nm radius), respectively.⁹⁸ These sizes are well within the range of sizes typically present in the nanoparticle sample.⁶

These single particle tracking experiments expand the realm of single nanoparticle spectroscopy to moving particles. Using the Stokes–Einstein relationship, nanoparticle sizes can be extracted. Although the frictional coefficient for a sphere was utilized as a first approximation in these experiments, including more complex frictional coefficients for other shapes will improve the size calculations. Ultimately, the measured diffusion coefficient should allow us to determine accurate size and shape parameters of the nanoparticles of interest. This method provides a unique approach for correlating structure and function.

b. “On-the-Fly” Lithography. Measuring nanoparticle diffusion simultaneously with the LSPR spectrum in solution allows us to move to more complex environments, like cells. However, the nanoparticle movement is not controlled. It is important to be able to not only measure optical properties of single nanoparticles but also control the nanoparticle position. While utilizing the through-the-objective white light TIR geometry to spatially correlate optical and structural properties, Stiles and Willets et al.⁵⁸ demonstrated the ability to manipulate the position of a single nanoparticle by pushing it controllably with the AFM tip. Figure 13 depicts the controlled movement. In each frame, the AFM tip is visible among diffraction-limited spots (nanoparticles). The nanoparticle manipulation described here is an important development for “on-the-fly” lithography and is a significant tool to be able to move nanoparticles controllably. In contrast to scanning tunneling microscopy that requires ultra-high vacuum, this on-the-fly lithography technique occurs in ambient conditions. Additionally, unlike e-beam lithography that fabricates fixed structures, these structures are dynamic. Although it is still at the early stages of development, this technique has a variety of potential applications for fabricating plasmonic structures with a range of shapes and sizes.

c. Limitations. Single nanoparticle spectroscopy coupled with structural analysis has been shown throughout this paper to be an invaluable tool for systematic nanoparticle characterization. However, this technique is not without limitations. The first intrinsic

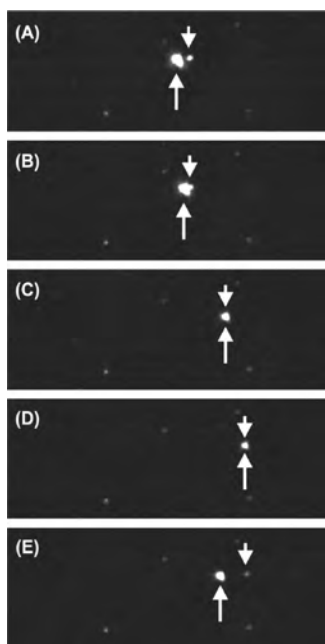


Figure 13. Series of images showing AFM tip–nanoparticle movement. (A) The tip is to the left of the nanoparticle. (B) The tip moves over the nanoparticle. (C) The tip and nanoparticle move. (D) The tip and nanoparticle are stopped at a certain position. (E) The tip moves away from the nanoparticle. The nanoparticle has moved from its original position in panel A. (Reproduced from ref 58.)

limitation from measuring the scattering of a plasmonic nanoparticle by dark-field microscopy comes from the size of the nanoparticle itself. As particles get smaller, the absorption becomes more important than the scattering since the scattering cross-section of a nanoparticle of radius a varies as a^6 , whereas its absorption varies as a^3 .¹⁸ Methods for correlating the absorption⁹⁹ and the extinction¹⁰⁰ of nanoparticles as small as 5 nm have been recently developed.

Second, the large surface to volume ratio for nanoparticles leads to some structural instability under an electron beam.¹⁰¹ As a consequence, nanoparticles may undergo crystallographic rearrangement accompanied by a change of shape (for single particles) and coalescence (for nanoparticle aggregates). For structural characterization techniques utilizing SEM or TEM, the optical properties must be measured before the nanoparticles are in contact with the electron beam. It has been observed that the LSPR changes before and after TEM imaging (Figure 14). Additionally, SERS is not observed after TEM imaging of nanostructures that previously exhibited it,⁸⁷ likely due to radiolytic damage^{102,103} of the Raman-active molecules. Structural and optical characterization of nanoparticles is a useful technique; however, based on the experimental observations exemplified in Figure 14, the nanoparticle samples can be probed only once by TEM. Ultimately, there is a need to protect the nanoparticle from environmental influences, like solvents, heat, electron beams, and oxidation, while maintaining its structural and functional integrity. There have been many recent advances in TEM instrumentation, including optical correctors, reduction of the beam voltage, as well as improvements in sample holders, which may be able to overcome these limitations.

VII. SUMMARY AND OUTLOOK

Throughout this article, we have described some of the methods and instrumentation developments that enable one to correlate the

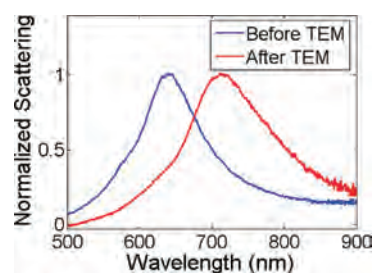


Figure 14. Scattering spectra of the same Au nanoparticle (decahedron) before (blue curve) and after (red curve) performing TEM, illustrating the effect of electron beam exposure. The red shift was observed reproducibly for Au nanoparticles.

structural and optical properties of metal nanoparticles, specifically Ag and Au. However, recent work has demonstrated the plasmonic activity of other metals, like Cu⁴¹, Al⁴³, Pt and Pd,^{104,105} expanding the realm of possibilities for chemists and materials scientists. Although ensemble measurements might be representative of structural differences between nanoparticle samples, only single nanoparticle measurements can reflect the optical dispersion in a sample. Recent progress in the instrumentation based on dark-field spectroscopy has allowed the study of nano-objects ranging from carbon nanotubes^{106,107} to metallic nanoparticles. One example of application is the tracking of the diffusion of metallic nanoparticles, opening the road to in vivo LSPR sensing. Overall, the recent progress presented here paves the way for the use of nanoparticles as individual sensors.

AUTHOR INFORMATION

Corresponding Author

*E-mail: vanduyne@northwestern.edu.

BIOGRAPHIES



Anne-Isabelle Henry received a B.S. in physical chemistry from University Paris Sud (2003) in Orsay, France, after completing a research internship at the Fritz Haber Institute in Berlin, Germany, with Dr. T. Hertel. She received her Ph.D. (2008) in chemistry from University Pierre and Marie Curie in Paris, France, advised by Profs. M.P. Pileni and A. Courty. She is currently a postdoctoral fellow at Northwestern University in the groups of Profs. R. P. Van Duyne and G. C. Schatz. Her research interests include the fabrication, assembly, and study of plasmonic nanoparticles, SERS-active nanoparticle clusters, and substrates.



Julia M. Bingham received her B.S. in chemistry from The Pennsylvania State University—Schreyer Honors College in State College, PA. She received her Ph.D. in chemistry from Northwestern University in Evanston, IL, advised by Prof. Richard P. Van Duyne. She is currently a postdoctoral researcher at Northwestern University in the Van Duyne group. Her research focuses on single nanoparticle imaging and spectroscopy on both stationary and moving nanoparticles.



Emilie Ringe is a Ph.D. candidate in the groups of Profs. L. D. Marks and R. P. Van Duyne at Northwestern University. She studied at McGill University at the undergraduate level before she obtained a M.S. from Northwestern University in inorganic crystallography with J. A. Ibers. Her current interests are broadly defined as the structure–property relationships in metal nanoparticles, inorganic crystals, and other materials.



Laurence D. Marks received his B.A. in chemistry and a Ph.D. in physics from Cambridge University. Marks did postdoctoral

training in Cambridge with Drs. D. J. Smith and A. Howie as well as with Prof. J. M. Cowley at Arizona State University. Since 1985 he has been a faculty member at Northwestern University. He has research interests in a range of areas, from nanoparticles to nanotribology and surface science.



George C. Schatz is Charles E. and Emma H. Morrison Professor of Chemistry and of Chemical and Biological Engineering at Northwestern University. He received a B.S. (1971) at Clarkson University and Ph.D. (1976) at Caltech, both in chemistry. He was a postdoc at MIT and has been at Northwestern since 1976. Schatz is a member of the National Academy of Sciences, the American Academy of Arts and Sciences, and the International Academy of Quantum Molecular Sciences, and he is Editor-in-Chief of the *Journal of Physical Chemistry*. He has contributed to theory and modeling in many areas of nanoscience.



Richard P. Van Duyne is Charles E. and Emma H. Morrison Professor of Chemistry and of Biomedical Engineering at Northwestern University. He received a B.S. (1967) at the Rensselaer Polytechnic Institute and Ph.D. (1971) at the University of North Carolina, Chapel Hill, both in chemistry. Van Duyne is a member of the National Academy of Sciences and the American Academy of Arts and Sciences. He is known for the discovery of surface-enhanced Raman spectroscopy (SERS), the invention of nanosphere lithography (NSL), and development of ultrasensitive nanosensors based on localized surface plasmon resonance (LSPR) spectroscopy.

■ ACKNOWLEDGMENT

This research was supported by the AFOSR/DARPA Project BAA07-61 (FA9550-08-1-0221), the NSF (CHE-0414554,

CHE-0911145, and CHE-1025941), the NSF Network for Computational Nanotechnology, and the NSF MRSEC (DMR-0520513) at the Materials Research Center of Northwestern University.

REFERENCES

- (1) Talapin, D. V.; Lee, J.-S.; Kovalenko, M. V.; Shevchenko, E. V. *Chem. Rev.* **2010**, *110*, 389–458.
- (2) Burda, C.; Chen, X.; Narayanan, R.; El-Sayed, M. A. *Chem. Rev.* **2005**, *105*, 1025–1102.
- (3) Wiley, B.; Sun, Y.; Xia, Y. *Acc. Chem. Res.* **2007**, *40*, 1067–1076.
- (4) Courty, A.; Henry, A.-I.; Goubet, N.; Pileni, M. P. *Nat. Mater.* **2007**, *6*, 900–907.
- (5) Henzie, J.; Lee, J.; Lee, M. H.; Hasan, W.; Odom, T. W. *Annu. Rev. Phys. Chem.* **2009**, *60*, 147–165.
- (6) Jin, R. C.; Cao, Y. W.; Mirkin, C. A.; Kelly, K. L.; Schatz, G. C.; Zheng, J. G. *Science* **2001**, *294*, 1901–1903.
- (7) Haynes, C. L.; Van Duyne, R. P. *J. Phys. Chem. B* **2001**, *105*, 5599–5611.
- (8) Millstone, J. E.; Hurst, S. J.; Metraux, G. S.; Cutler, J. I.; Mirkin, C. A. *Small* **2009**, *5*, 646–664.
- (9) Park, J.; Joo, J.; Kwon, S. G.; Jang, Y.; Hyeon, T. *Angew. Chem., Int. Ed.* **2007**, *46*, 4630–4660.
- (10) Pileni, M. P. *J. Phys. Chem. C* **2007**, *111*, 9019–9038.
- (11) Tao, A. R.; Habas, S.; Yang, P. *Small* **2008**, *4*, 310–325.
- (12) Grzelczak, M.; Perez-Juste, J.; Mulvaney, P.; Liz-Marzan, L. M. *Chem. Soc. Rev.* **2008**, *37*, 1783–1791.
- (13) Lee, J.; Hasan, W.; Stender, C. L.; Odom, T. W. *Acc. Chem. Res.* **2008**, *41*, 1762–1771.
- (14) El-Sayed, M. A. *Acc. Chem. Res.* **2004**, *37*, 326–333.
- (15) Jain, P. K.; Huang, X.; El-Sayed, I. H.; El-Sayed, M. A. *Acc. Chem. Res.* **2008**, *41*, 1578–1586.
- (16) Murphy, C. J.; Sau, T. K.; Gole, A. M.; Orendorff, C. J.; Gao, J.; Gou, L.; Hunyadi, S. E.; Li, T. *J. Phys. Chem. B* **2005**, *109*, 13857–13870.
- (17) Pileni, M. P. *Acc. Chem. Res.* **2008**, *41*, 1799–1809.
- (18) Mie, G. *Ann. Phys.* **1908**, *25*, 377–445.
- (19) Gans, R. *Ann. Phys.* **1912**, *342*, 881–900.
- (20) Gans, R. *Ann. Phys.* **1915**, *352*, 270–284.
- (21) Willets, K. A.; Van Duyne, R. P. *Annu. Rev. Phys. Chem.* **2007**, *58*, 267–297.
- (22) Anker, J. N.; Hall, W. P.; Lyandres, O.; Shah, N. C.; Zhao, J.; Van Duyne, R. P. *Nat. Mater.* **2008**, *7*, 442–453.
- (23) Hall, W. P.; Anker, J. N.; Lin, Y.; Modica, J.; Mirkin, M.; Van Duyne, R. P. *J. Am. Chem. Soc.* **2008**, *130*, 5836–5837.
- (24) Kreno, L. E.; Hupp, J. T.; Van Duyne, R. P. *Anal. Chem.* **2010**, *82*, 8042–8046.
- (25) Bingham, J. M.; Anker, J. N.; Kreno, L. E.; Van Duyne, R. P. *J. Am. Chem. Soc.* **2010**, *132*, 17358–17359.
- (26) Stiles, P. L.; Dieringer, J. A.; Shah, N. C.; Van Duyne, R. P. *Annu. Rev. Anal. Chem.* **2008**, *1*, 601–626.
- (27) Schatz, G. C.; Young, M. A.; Van Duyne, R. P. *Electromagnetic Mechanism of SERS*. In *Surface-Enhanced Raman Scattering*; Kneipp, K., Moskovits, M., Kneipp, H., Eds.; Springer: Berlin/Heidelberg, 2006; Vol. 103, pp 19–45.
- (28) Fort, E.; Grésillon, S. *J. Phys. D: Appl. Phys.* **2008**, *41*, 013001.
- (29) Jensen, T. R.; Van Duyne, R. P.; Johnson, S. A.; Maroni, V. A. *Appl. Spectrosc.* **2000**, *54*, 371–377.
- (30) Le Ru, E. C.; Blackie, E.; Meyer, M.; Etchegoin, P. G. *J. Phys. Chem. C* **2007**, *111*, 13794–13803.
- (31) Zsigmondy, R. *Nobel Lectures, Chemistry 1922–1941*; Elsevier Publishing Company: Amsterdam, 1966.
- (32) Sönnichsen, C.; Geier, S.; Hecker, N.; Von Plessen, G.; Feldmann, J.; Dittbacher, H.; Lamprecht, B.; Krenn, J.; Aussenegg, F.; Chan, V. *Appl. Phys. Lett.* **2000**, *77*, 2949–2951.
- (33) Sönnichsen, C.; Franzl, T.; Wilk, T.; Von Plessen, G.; Feldmann, J.; Wilson, O.; Mulvaney, P. *Phys. Rev. Lett.* **2002**, *88*, 77402.
- (34) Schultz, S.; Smith, D. R.; Mock, J. J.; Schultz, D. A. *Proc. Natl. Acad. Sci. U.S.A.* **2000**, *97*, 996–1001.
- (35) Mock, J. J.; Barbic, M.; Smith, D. R.; Schultz, D. A.; Schultz, S. *J. Chem. Phys.* **2002**, *116*, 6755–6759.
- (36) Nie, S.; Emory, S. R. *Science* **1997**, *275*, 1102–1106.
- (37) Hulsteen, J. C.; Van Duyne, R. P. *J. Vac. Sci. Technol., A* **1995**, *13*, 1553–1558.
- (38) Hulsteen, J. C.; Treichel, D. A.; Smith, M. T.; Duval, M. L.; Jensen, T. R.; Van Duyne, R. P. *J. Phys. Chem. B* **1999**, *103*, 3854–3863.
- (39) Duval Malinsky, M.; Kelly, K. L.; Schatz, G. C.; Van Duyne, R. P. *J. Phys. Chem. B* **2001**, *105*, 2343–2350.
- (40) Haynes, C. L.; Van Duyne, R. P. *J. Phys. Chem. B* **2003**, *107*, 7426–7433.
- (41) Chan, G. H.; Zhao, J.; Hicks, E. M.; Schatz, G. C.; Van Duyne, R. P. *Nano Lett.* **2007**, *7*, 1947–1952.
- (42) Whitney, A. V.; Elam, J. W.; Stair, P. C.; Van Duyne, R. P. *J. Phys. Chem. C* **2007**, *111*, 16827–16832.
- (43) Chan, G. H.; Zhao, J.; Schatz, G. C.; Van Duyne, R. P. *J. Phys. Chem. C* **2008**, *112*, 13958–13963.
- (44) Ormonde, A. D.; Hicks, E. C. M.; Castillo, J.; Van Duyne, R. P. *Langmuir* **2004**, *20*, 6927–6931.
- (45) Jensen, T. R.; Duval, M. L.; Kelly, K. L.; Lazarides, A. A.; Schatz, G. C.; Van Duyne, R. P. *J. Phys. Chem. B* **1999**, *103*, 9846–9853.
- (46) Sung, J.; Kosuda, K. M.; Zhao, J.; Elam, J. W.; Spears, K. G.; Van Duyne, R. P. *J. Phys. Chem. C* **2008**, *112*, 5707–5714.
- (47) Jensen, T. R.; Duval, M. L.; Kelly, K. L.; Lazarides, A. A.; Schatz, G. C.; Van Duyne, R. P. *J. Phys. Chem. B* **1999**, *103*, 9846–9853.
- (48) Jensen, T. R.; Duval Malinsky, M.; Haynes, C. L.; Van Duyne, R. P. *J. Phys. Chem. B* **2000**, *104*, 10549–10556.
- (49) Zhang, X.; Hicks, E. M.; Zhao, J.; Schatz, G. C.; Van Duyne, R. P. *Nano Lett.* **2005**, *5*, 1503–1507.
- (50) Ormonde, A. D.; Hicks, E. C. M.; Castillo, J.; Van Duyne, R. P. *Langmuir* **2004**, *20*, 6927–6931.
- (51) McFarland, A. D.; Van Duyne, R. P. *Nano Lett.* **2003**, *3*, 1057–1062.
- (52) Mock, J. J.; Smith, D. R.; Schultz, S. *Nano Lett.* **2003**, *3*, 485–491.
- (53) Raschke, G.; Kowarik, S.; Franzl, T.; Sönnichsen, C.; Klar, T. A.; Feldmann, J.; Nichtl, A.; Kurzinger, K. *Nano Lett.* **2003**, *3*, 935–938.
- (54) Sherry, L. J.; Chang, S.-H.; Schatz, G. C.; Van Duyne, R. P.; Wiley, B. J.; Xia, Y. *Nano Lett.* **2005**, *5*, 2034–2038.
- (55) Sherry, L. J.; Jin, R.; Mirkin, C. A.; Schatz, G. C.; Van Duyne, R. P. *Nano Lett.* **2006**, *6*, 2060–2065.
- (56) Knight, M. W.; Wu, Y.; Lassiter, J. B.; Nordlander, P.; Halas, N. J. *Nano Lett.* **2009**, *9*, 2188–2192.
- (57) Kelly, K. L.; Coronado, E.; Zhao, L. L.; Schatz, G. C. *J. Phys. Chem. B* **2003**, *107*, 668–677.
- (58) Stiles, R. L.; Willets, K. A.; Sherry, L. J.; Roden, J. M.; Van Duyne, R. P. *J. Phys. Chem. C* **2008**, *112*, 11696–11701.
- (59) Axelrod, D.; Hellen, E. H.; Fulbright, R. M. Total internal reflection fluorescence. In *Topics in Fluorescence Spectroscopy*; Lakowicz, J., Ed.; Plenum: New York, 1992; Vol. 3, pp 289–343.
- (60) Sarkar, A.; Robertson, R. B.; Fernandez, J. M. *Proc. Natl. Acad. Sci. U.S.A.* **2004**, *101*, 12882–12886.
- (61) Piner, R. D.; Zhu, J.; Xu, F.; Hong, S.; Mirkin, C. A. *Science* **1999**, *283*, 661–663.
- (62) Salaita, K.; Wang, Y.; Mirkin, C. A. *Nat. Nanotechnol.* **2007**, *2*, 145–155.
- (63) Novo, C.; Funston, A. M.; Pastoriza-Santos, I.; Liz-Marzán, L. M.; Mulvaney, P. *Angew. Chem., Int. Ed.* **2007**, *46*, 3517–3520.
- (64) Mock, J. J.; Barbic, M.; Smith, D. R.; Schultz, D. A.; Schultz, S. *J. Chem. Phys.* **2002**, *116*, 6755–6759.
- (65) Wang, Y.; Eswaramoorthy, S. K.; Sherry, L. J.; Dieringer, J. A.; Camden, J. P.; Schatz, G. C.; Van Duyne, R. P.; Marks, L. D. *Ultra-microscopy* **2009**, *109*, 1110–1113.
- (66) McMahon, J. M.; Wang, Y.; Sherry, L. J.; Van Duyne, R. P.; Marks, L. D.; Gray, S. K.; Schatz, G. C. *J. Phys. Chem. C* **2009**, *113*, 2731–2735.

- (67) Rodriguez-Fernandez, J.; Novo, C.; Myroshnychenko, V.; Funston, A. M.; Sanchez-Iglesias, A.; Pastoriza-Santos, I.; Perez-Juste, J.; Garcia de Abajo, F. J.; Liz-Marzan, L. M.; Mulvaney, P. *J. Phys. Chem. C* **2009**, *113*, 18623–18631.
- (68) Tcherniak, A.; Ha, J. W.; Dominguez-Medina, S.; Slaughter, L. S.; Link, S. *Nano Lett.* **2010**, *10*, 1398–1404.
- (69) Munechika, K.; Smith, J. M.; Chen, Y.; Ginger, D. S. *J. Phys. Chem. C* **2007**, *111*, 18906–18911.
- (70) Nelayah, J.; Kociak, M.; Stéphan, O.; Geuquet, N.; Henrard, L.; Garcia de Abajo, F. J.; Pastoriza-Santos, I.; Liz-Marzan, L. M.; Colliex, C. *Nano Lett.* **2010**, *10*, 902–907.
- (71) Hu, M.; Chen, J.; Marquez, M.; Xia, Y.; Hartland, G. V. *J. Phys. Chem. C* **2007**, *111*, 12558–12565.
- (72) Ringe, E.; McMahon, J. M.; Sohn, K.; Cobley, C.; Xia, Y.; Huang, J.; Schatz, G. C.; Marks, L. D.; Van Duyne, R. P. *J. Phys. Chem. C* **2010**, *114*, 12511–12516.
- (73) Myroshnychenko, V.; Rodriguez-Fernandez, J.; Pastoriza-Santos, I.; Funston, A. M.; Novo, C.; Mulvaney, P.; Liz-Marzan, L. M.; Garcia de Abajo, F. J. *Chem. Soc. Rev.* **2008**, *37*, 1792–1805.
- (74) Svedendahl, M.; Chen, S.; Dmitriev, A.; Käll, M. *Nano Lett.* **2009**, *9*, 4428–4433.
- (75) Louit, G.; Asahi, T.; Tanaka, G.; Uwada, T.; Masuhara, H. *J. Phys. Chem. C* **2009**, *113*, 11766–11772.
- (76) Bingham, J.; Willets, K.; Shah, N.; Andrews, D.; Van Duyne, R. *J. Phys. Chem. C* **2009**, *113*, 16839–16842.
- (77) Wustholz, K. L.; Henry, A.-I.; Bingham, J. M.; Kleinman, S. L.; Natan, M. J.; Freeman, R. G.; Van Duyne, R. P. Exploring single-molecule SERS and single-nanoparticle plasmon microscopy. *Proc. SPIE* **2009**, 739403–10.
- (78) Lee, P. C.; Meisel, D. *J. Phys. Chem.* **1982**, *86*, 3391–3395.
- (79) Camden, J. P.; Dieringer, J. A.; Wang, Y.; Masiello, D. J.; Marks, L. D.; Schatz, G. C.; Van Duyne, R. P. *J. Am. Chem. Soc.* **2008**, *130*, 12616–12617.
- (80) Jeanmaire, D. L.; Van Duyne, R. P. *J. Electroanal. Chem.* **1977**, *84*, 1–20.
- (81) Dieringer, J. A.; Lettan, R. B.; Scheidt, K. A.; Van Duyne, R. P. *J. Am. Chem. Soc.* **2007**, *129*, 16249–16256.
- (82) Moskovits, M. *Rev. Mod. Phys.* **1985**, *57*, 783–826.
- (83) Metiu, H.; Das, P. *Annu. Rev. Phys. Chem.* **1984**, *35*, 507–536.
- (84) Michaels, A. M.; Nirmal, M.; Brus, L. E. *J. Am. Chem. Soc.* **1999**, *121*, 9932–9939.
- (85) Michaels, A. M.; Jiang, J.; Brus, L. *J. Phys. Chem. B* **2000**, *104*, 11965–11971.
- (86) Kleinman, S. L.; Ringe, E.; Valley, N.; Wustholz, K. L.; Phillips, E.; Scheidt, K. A.; Schatz, G. C.; Van Duyne, R. P. *J. Am. Chem. Soc.* **2011**, *133*, 4115–4122.
- (87) Wustholz, K. L.; Henry, A.-I.; McMahon, J. M.; Freeman, R. G.; Valley, N.; Piotti, M. E.; Natan, M. J.; Schatz, G. C.; Duyne, R. P. *J. Am. Chem. Soc.* **2010**, *132*, 10903–10910.
- (88) Doering, W. E.; Piotti, M. E.; Natan, M. J.; Freeman, R. G. *Adv. Mater.* **2007**, *19*, 3100–3108.
- (89) Tyler, T. P.; Henry, A.-I.; Van Duyne, R. P.; Hersam, M. C. *J. Phys. Chem. Lett.* **2011**, *2*, 218–222.
- (90) McMahon, J. M.; Henry, A.-I.; Wustholz, K. L.; Natan, M. J.; Freeman, R. G.; Van Duyne, R. P.; Schatz, G. C. *Anal. Bioanal. Chem.* **2009**, *394*, 1819–1825.
- (91) Saxton, M. J. *Biophys. J.* **1997**, *72*, 1744–1753.
- (92) Saxton, M. J.; Jacobson, K. *Annu. Rev. Biophys. Biomol. Struct.* **1997**, *26*, 373–399.
- (93) Qian, H.; Sheetz, M. P.; Elson, E., L. *Biophys. J.* **1991**, *60*, 910–921.
- (94) Vrljic, M.; Nishimura, S. Y.; Brasselet, S.; Moerner, W. E.; McConnell, H. M. *Biophys. J.* **2002**, *83*, 2681–2692.
- (95) Vrljic, M.; Nishimura, S. Y.; Moerner, W. E.; McConnell, H. M. *Biophys. J.* **2005**, *88*, 334–347.
- (96) Suzuki, K. G. N.; Fujiwara, T. K.; Sanematsu, F.; Iino, R.; Edidin, M.; Kusumi, A. *J. Cell Biol.* **2007**, *177*, 717–730.
- (97) Nallathamby, P. D.; Lee, K., J.; Xu, X.-H. N. *ACS Nano* **2008**, *2*, 1371–1380.
- (98) Kleinman, S. L.; Bingham, J. M.; Henry, A.-I.; Wustholz, K. L.; Van Duyne, R. P. Structural and optical characterization of single nanoparticle and single molecule SERS. *Proc. SPIE - Int. Soc. Opt. Eng.* **2010**, 77570J-1–10.
- (99) Van Dijk, M. A.; Tchebotareva, A. L.; Orrit, M.; Lippitz, M.; Berciaud, S.; Lasne, D.; Cognet, L.; Lounis, B. *Phys. Chem. Chem. Phys.* **2006**, *8*, 3486–3495.
- (100) Billaud, P.; Marhaba, S.; Cottancin, E.; Arnaud, L.; Bachelier, G.; Bonnet, C.; Del Fatti, N.; Lerme, J.; Vallée, F.; Vialle, J. L.; Broyer, M.; Pellarin, M. *J. Phys. Chem. C* **2008**, *112*, 978–982.
- (101) Ajayan, P. M.; Marks, L. D. *Phys. Rev. Lett.* **1989**, *63*, 279–282.
- (102) Buckett, M. I.; Strane, J.; Luzzi, D. E.; Zhang, J. P.; Wessels, B. W.; Marks, L. D. *Ultramicroscopy* **1989**, *29*, 217–227.
- (103) Egerton, R. F.; Li, P.; Malac, M. *Micron* **2004**, *35*, 399–409.
- (104) Langhammer, C.; Yuan, Z.; Zoric, I.; Kasemo, B. *Nano Lett.* **2006**, *6*, 833–838.
- (105) Langhammer, C.; Kasemo, B.; Zoric, I. *J. Chem. Phys.* **2007**, *126*, 194702.
- (106) Wang, F.; Sfeir, M. Y.; Huang, L.; Huang, X.; Huang, X. M. H.; Wu, Y.; Kim, J.; Hone, J.; O'Brien, S.; Brus, L. E.; Heinz, T. F. *Phys. Rev. Lett.* **2006**, *96*, 167401.
- (107) Joh, D. Y.; Herman, L. H.; Ju, S.-Y.; Kinder, J.; Segal, M. A.; Johnson, J. N.; Chan, G. K. L.; Park, J. *Nano Lett.* **2011**, *11*, 1–7.